

Supplementary Information

Fluorine Substitution Enabling Pseudocapacitive Intercalation of Sodium Ions in Niobium Oxyfluoride

Yilan Wu,^a Xin Fan,^a Yinjuan Chen,^{b,c} Rohit Ranganathan Gaddam,^a Feng Yu,^d Changlong Xiao,^a Chunfu Lin,^e Qinglan Zhao,^a Xiaoming Sun,^a Hongxia Wang,^d Chenguang Liu,^b Jun Li,^c Xiu Song Zhao^{a,e,}*

^a School of Chemical Engineering, The University of Queensland, St Lucia, Brisbane, QLD 4072, Australia

^b State Key Laboratory of Heavy Oil Processing, China University of Petroleum (East China), Qingdao, 266580, China

^c Department of Chemistry, Tsinghua University, Beijing 100084, China

^d School of Chemistry, Physics and Mechanical Engineering, Science and Engineering Faculty, Queensland University of Technology, Brisbane, QLD, 4001, Australia

^e Institute of Materials for Energy and Environment, College of Materials Science and Engineering, Qingdao University, 308 Ningxia Road, Qingdao, 266071, China

E-mail address: george.zhao@uq.edu.au

Experimental section

Synthesis of $T\text{-Nb}_2\text{O}_{5-x}\text{F}_y\text{C-NBs}$

All the reagents used were of analytical grade and used as received without purification. The $T\text{-Nb}_2\text{O}_{5-x}\text{F}_y\text{C-NBs}$ sample was prepared using an ethanol-assisted solvothermal synthesis method. Typically, 1.0 mL of hydrofluoric acid (Sigma 50 wt. %) was added into 30 mL of ethylene glycol (Sigma 98%) under magnetic stirring for 0.5 h. Then, 150 mg of niobium powder (Sigma 98.5 %) was added into the above solution. After ultrasonication and magnetic stirring for 1 h, the mixture was transferred into a 50 mL Teflon-lined stainless steel autoclave, followed by hydrothermal treatment at 160 °C for 24 h. After cooling down naturally to room temperature, the bluish green precipitate was collected by filtration, washing with ethanol and deionised water. The sample was freeze-dried for 48 h, followed by annealing at 800 °C for 2 h under nitrogen flow in a tube furnace to obtain sample $T\text{-Nb}_2\text{O}_{5-x}\text{F}_y\text{C-NBs}$.

Synthesis of $T\text{-Nb}_2\text{O}_5\text{C}$

Typically, 150 mg niobium (V) chloride (Sigma 99.9%) was dissolved in 30 mL ethanol under vigorous stirring. After that, 1.5 mL oleylamine (Sigma 98%) was added into the above solution, and then heated at 75 °C for 6 h in an oil bath under stirring. The white product was collected by centrifugation and then washed with ethanol and deionised water for several times. The dried sample was subsequently annealing at 800 °C for 2 h under nitrogen flow, and is denoted as $T\text{-Nb}_2\text{O}_5\text{C}$.

Characterisation

X-ray diffraction (XRD) patterns were collected on a Bruker D8 Advance X-ray diffractometer (Cu $K\alpha$ radiation, $\lambda = 1.54056 \text{ \AA}$). *Operando* XRD patterns were acquired on a Rigaku SmartLab X-ray diffractometer with Cu $K\alpha$ radiation ($\lambda = 1.5406 \text{ \AA}$). The electrode was loaded in the XRD cell (equipped with a Beryllium window) in an argon-filled glovebox. The XRD cell unit was connected to a SP150 (Biologic, France) single-channel potentiostat for charging/discharging during XRD measurements. The electrochemical measurements were carried out at a current density of 0.02 A g^{-1} and at a XRD scanning rate of $0.5^\circ (2\theta) \text{ min}^{-1}$. The morphology of samples was examined on a field-emission scanning electron microscope (FESEM, JEOL 7001) at 10 kV. Transmission electron microscopy (TEM) and high-resolution TEM (HRTEM) measurements were conducted on a JEOL-JEM-2100F microscope equipped with an energy dispersive X-ray (EDX). X-ray photoelectron spectroscopy (XPS) spectra were acquired on a Kratos Axis photoelectron spectrometer equipped with an Al ($K\alpha$ 1486.6 eV)

radiation. The cluster beam used had a beam energy of 4 keV and the cluster size was 1000 atoms for etching.

For *ex situ* TEM and XPS measurements, electrode samples were collected from coin cells that were cycled to the desirable potentials (*vs.* Na/Na⁺) in a glovebox, and stored in an argon-filled container for XPS measurements. Nitrogen adsorption/desorption isotherms were measured on a Tristar II 3020 instrument at 77 K. Samples were degassed at 150 °C overnight before measurements of nitrogen adsorption. Thermogravimetric analysis (TGA) was performed on a DTA-TG apparatus (Shimadzu, DTG-60A).

Electrochemical measurements

Electrodes were prepared by mixing an active material, carbon black and polyvinylidene fluoride (PVDF) at a mass ratio of 7:2:1 in *N*-methyl pyrrolidone (NMP) solvent under magnetic stirring to form a slurry, which was subsequently casted onto a current collector with a copper foil for the $T\text{-Nb}_2\text{O}_{5-x}\text{F}_y\text{-C-NBs}$ electrode and an aluminium foil for a commercial activated carbon (AC, BET surface area of 1293 m² g⁻¹) electrode using a doctor blade. The electrodes were dried at 80 °C overnight in a vacuum oven. The mass loadings of the active materials on the electrodes were about 0.8~1.0 mg cm⁻² for $T\text{-Nb}_2\text{O}_{5-x}\text{F}_y\text{-C-NBs}$, and about 2.5-3.0 mg cm⁻² for AC, respectively. The diameter of the electrodes was 1.0 cm. Sodium-ion battery cells were assembled using the working electrode, glass fibre separator (GF/D, Whatman) and sodium metal counter electrode in 2032-type coin cells. Sodium-ion capacitors were assembled using $T\text{-Nb}_2\text{O}_{5-x}\text{F}_y\text{-C-NBs}$ as anode and AC as cathode. Before assembling the full cells, the $T\text{-Nb}_2\text{O}_{5-x}\text{F}_y\text{-C-NBs}$ electrode was pre-cycled at 0.1 A g⁻¹ three times in a sodium half cell. To balance the capacity of the two electrodes, the mass ratio of the active materials of $T\text{-Nb}_2\text{O}_{5-x}\text{F}_y\text{-C-NBs}$ and AC was 1:3. The electrolyte consisted of 1.0 mol L⁻¹ sodium perchlorate (NaClO₄) in a mixture of ethylene carbonate (EC) and propylene carbonate (PC) (1:1 volume ratio) and 0.5 wt. % fluoroethylene carbonate (FEC). For *ex situ* TEM and XPS measurements, to ensure the system did not contain any other fluorine resources except that in the $T\text{-Nb}_2\text{O}_{5-x}\text{F}_y\text{-C-NBs}$, carboxymethyl cellulose (CMC) instead of PVDF was used as binder for electrode preparation. In addition, a mixture of PC/EC (1:1 volume ratio) without FEC was used as the electrolyte. The other procedures are the same as those for electrochemical measurements. The electrochemical properties of the samples were determined by using cyclic voltammetry (CV) and electrochemical impedance spectroscopy (EIS) on a VPM3 (Biologic, France). Galvanostatic charge-discharge measurements were conducted on a Neware battery

measurement system (CT3008). EIS measurements were performed at the open circuit potential before and after cycling over the frequency ranging from 0.01 Hz to 1 MHz.

The energy density and power density of the NIC full cells were calculated by using the following equations.

$$E = I * \int V dt \quad (1)$$

$$P = E/t \quad (2)$$

Where E (W h kg⁻¹) is the energy density, P (W kg⁻¹) is the power density, I (A g⁻¹) is the constant current density, V (V) is the working voltage, and t (s) is the discharge time. Note that the current density was obtained based on the total mass of both the positive and negative active materials.

DFT calculation details

The density functional theoretical (DFT) calculations were carried on by using the modified Perdew-Burke-Ernzerhof (PBEsol) functional within the formulation of generalized gradient approximation (GGA) as implemented in the DMOL³ program.¹⁻³ The Monkhorst-Pack scheme was used for sampling the Brillouin zone. The niobium electrons are described by semi-core pseudopotentials (DSPPs) and a double numerical plus polarization (DNP) basis set, while the light element including oxygen, fluorine, sodium-atoms are treated with all-electron basis sets. A Gaussian smearing finite-temperature broadening method (=0.005 a.u.) is used during structural optimisations. To ensure high-quality results, the real space atomic cutoff radius is chosen as 4.5 Å and the k-point is set as 3×1×5. Kohn-Sham self-consistent field calculations are performed with convergence tolerance of 1×10⁻⁶ a.u. on the total energy. The complete LST/QST protocol was used to the transition state (TS) search for the sodium-ion migration. Vibrational frequency analysis was performed to confirm the TS configuration.

The sodium ion adsorption energy is calculated by the following equation:

$$E_a = E(\text{slab_Na}^*) - (E(\text{slab}) + E(\text{Na})) \quad (3)$$

Where E_a represent the sodium ion adsorption energy, $E(\text{slab_Na}^*)$, $E(\text{slab})$ and $E(\text{Na})$ are the total energies of the sodium ion inserted $T\text{-Nb}_2\text{O}_{5-x}\text{F}_y$, the clear $T\text{-Nb}_2\text{O}_{5-x}\text{F}_y$ and the average total sodium atomic energy in the sodium unit cell. Similarly, the sodium ion adsorption energies of $T\text{-Nb}_2\text{O}_5$ were calculated based on the specific equation.

Since the atomic structure of $T\text{-Nb}_2\text{O}_5$ is highly complicated, a few approximations are applied on the models as described in the previous studies.⁴⁻⁵ The sodium ions are initially located at the three oxygen atoms or oxygen and fluorine atoms formed three-membered ring hollow sites

on 4g layer. The insertion of sodium ions leads to slight atomic rearrangement of the adjacent niobium and oxygen atoms on the 4h layer, which results in a six-membered ring. After geometry optimisation, sodium ions are stored at the sites where the total energy is minimised. As a result, the sodium ions are finally located at the exact hollow sites on the 4g layer and perpendicular to the six-membered ring centre sites of the 4h layer.

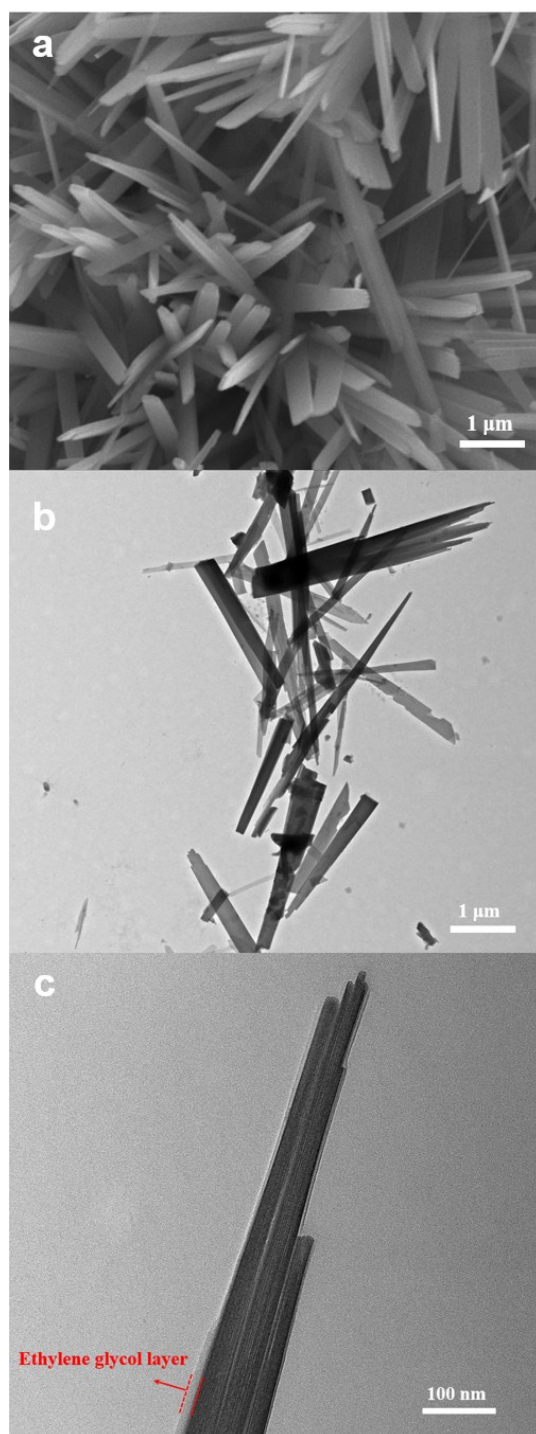


Figure S1. (a) FESEM image and (b, c) TEM images of the $T\text{-Nb}_2\text{O}_{5-x}\text{F}_y\text{-C-NBs}$ precursor

obtained from solvothermal synthesis.

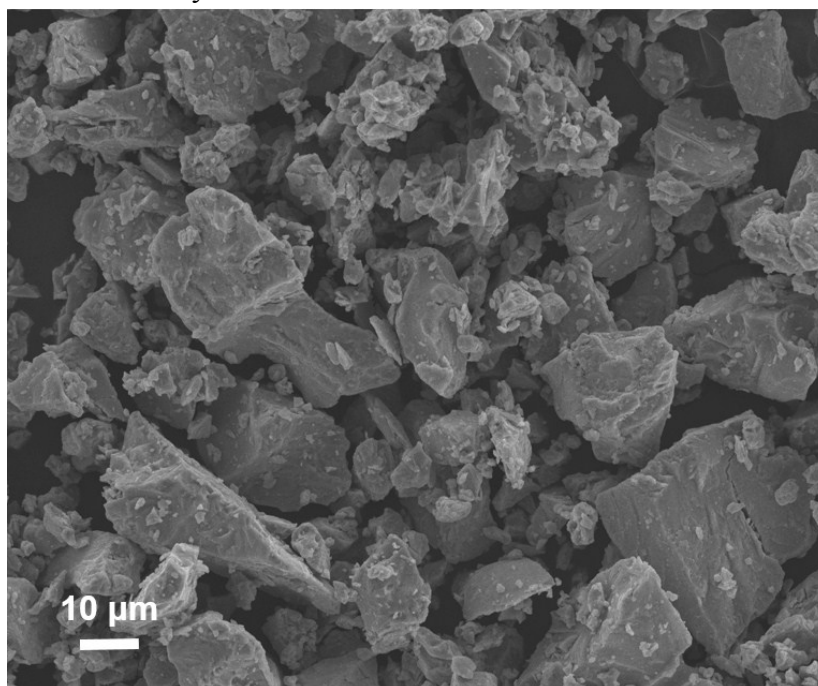


Figure S2. FESEM image of niobium powder used as the precursor for synthesising $T\text{-Nb}_2\text{O}_5\text{-}_x\text{F}_y\text{C-NBs}$.

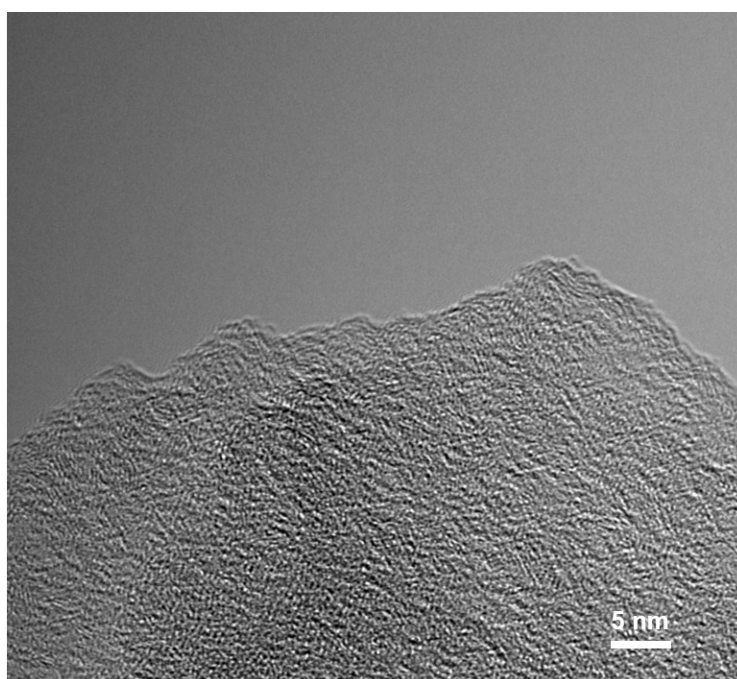


Figure S3. HRTEM image of the carbon belt in $T\text{-Nb}_2\text{O}_5\text{-}_x\text{F}_y\text{C-NBs}$.

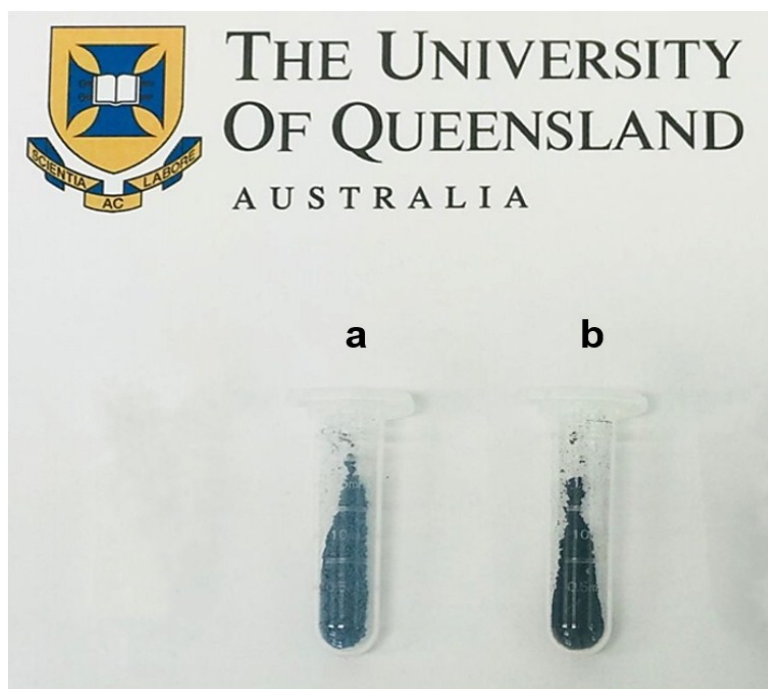


Figure S4. Digital photos of $T\text{-Nb}_2\text{O}_{5-x}\text{F}_y\text{C-NBs}$ before (a) and after (b) annealing at 800 °C for 2 h in a nitrogen atmosphere.

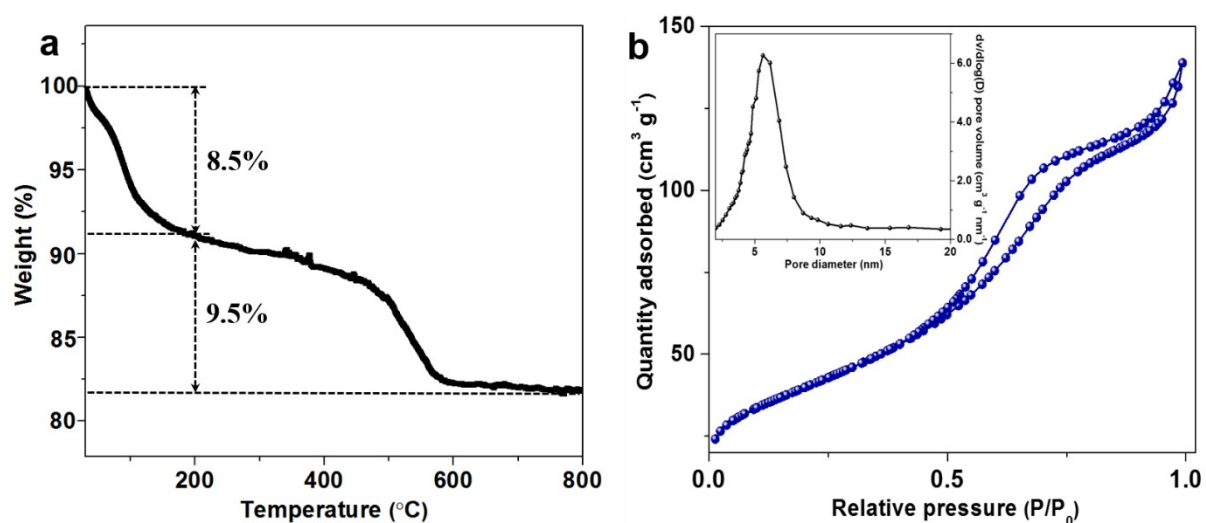


Figure S5. (a) TGA curve of $T\text{-Nb}_2\text{O}_{5-x}\text{F}_y\text{C-NBs}$ measured in air with a heating rate of 10 °C min⁻¹. **(b)** N₂ adsorption-desorption isotherms and BJH pore size distribution curve (inset).

Thermogravimetric analysis (TGA) was carried out to analyse the contents of carbon in $T\text{-Nb}_2\text{O}_{5-x}\text{F}_y\text{C-NBs}$. The weight loss below 200 °C was attributed to absorbed water. The weight loss between 200 and 800 °C (~ 10 wt. %) was due to carbon.

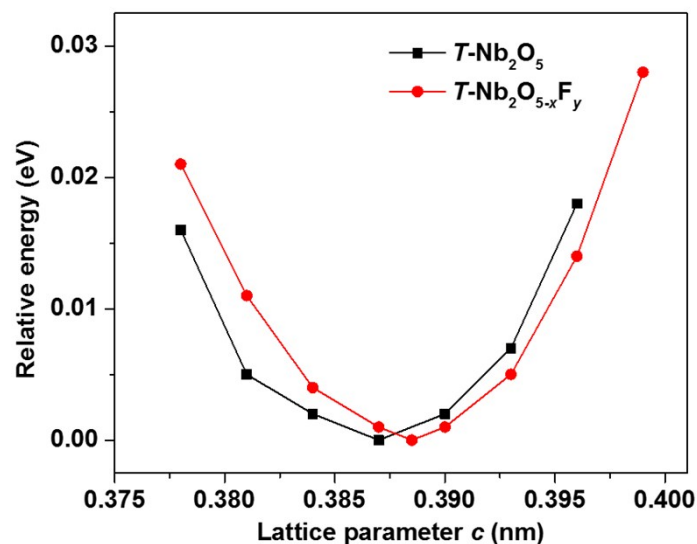


Figure S6. Relative energy (ΔE) as a function of lattice parameter c , illustrating the effect of substituted fluorine on the lattice parameter c . ΔE = the formation energy - the minimal energy.

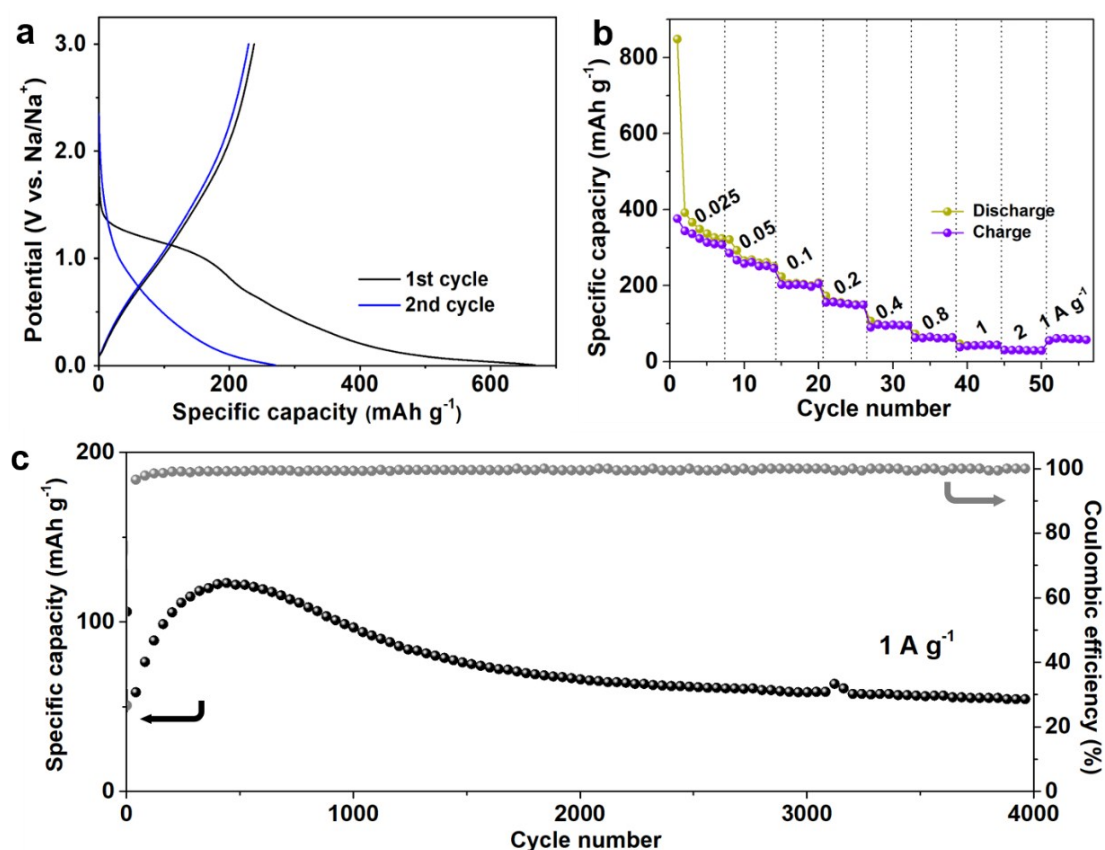


Figure S7. Electrochemical performance of $T\text{-Nb}_2\text{O}_5/\text{C}$ electrode for NIBs. **(a)** Galvanostatic discharge-charge profiles of the initial two cycles at 0.05 A g⁻¹. **(b)** Rate performance at various current densities from 0.025 to 2 A g⁻¹. **(c)** Cycling stability at a current density of 1 A g⁻¹.

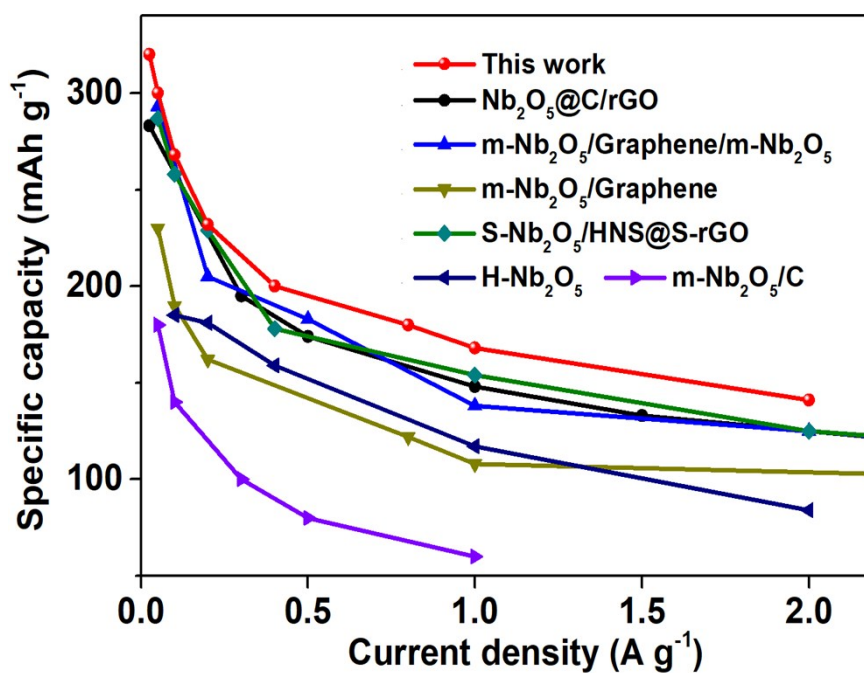


Figure S8. The comparison of rate performance of $T\text{-Nb}_2\text{O}_{5-x}\text{F}_y/\text{C-NBs}$ electrode with various recently reported $T\text{-Nb}_2\text{O}_5$ -based anodes for NIBs.

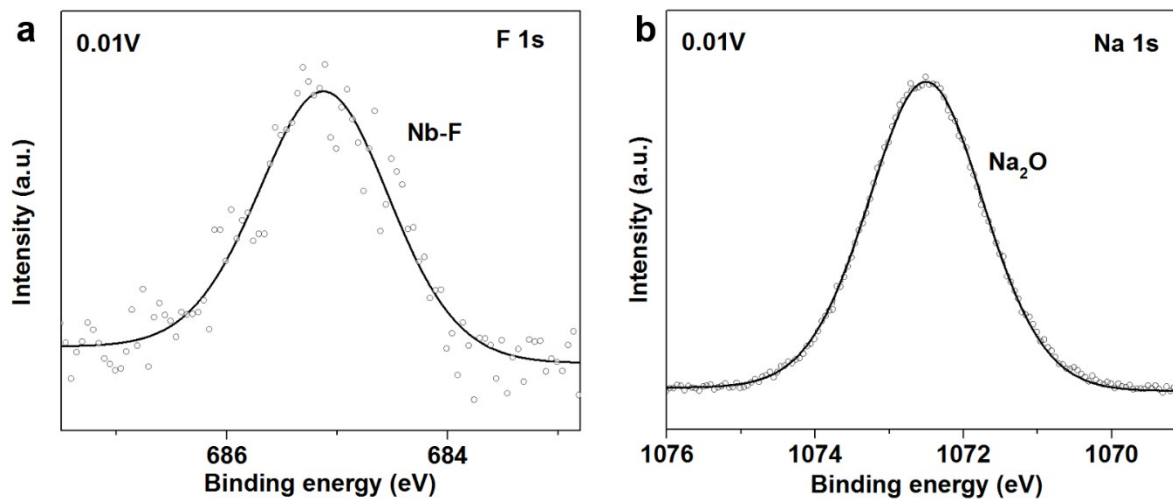


Figure S9. High-resolution XPS spectra of (a) F 1s and (b) Na 1s of electrode $T\text{-Nb}_2\text{O}_{5-x}\text{F}_y/\text{C-NBs}$ after being discharged to 0.01 V.

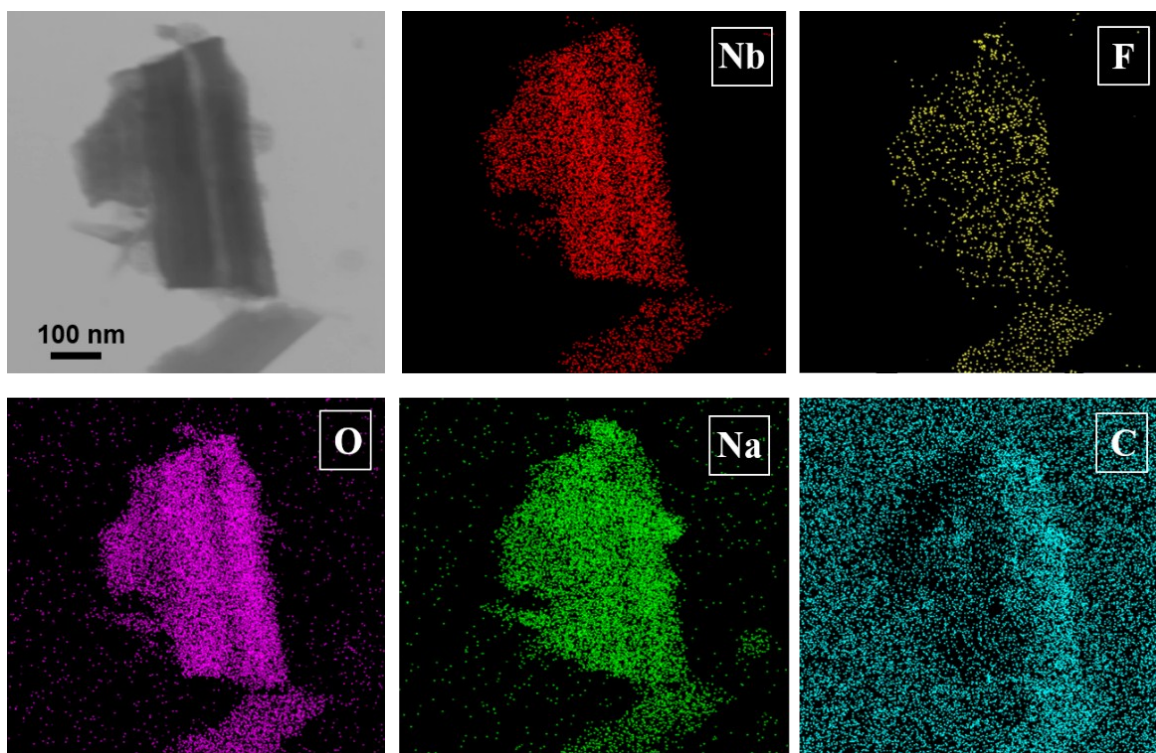


Figure S10. Elemental mapping images of electrode $T\text{-Nb}_2\text{O}_{5-x}\text{F}_y/\text{C-NBs}$ after 500 cycles in a sodium half cell, showing the distribution of niobium, fluorine, oxygen, sodium and carbon elements.

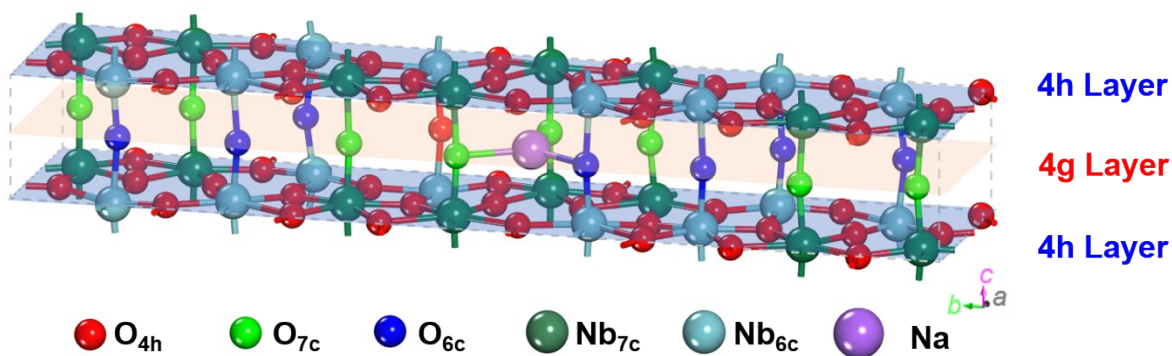


Figure S11. A sketch showing sodium ion location at the hollow site between the alternating 4h layers and coordinated with oxygen atoms in the 4g layers in $T\text{-Nb}_2\text{O}_5$ (corresponding to Site 1 or 2 in Figure 7).

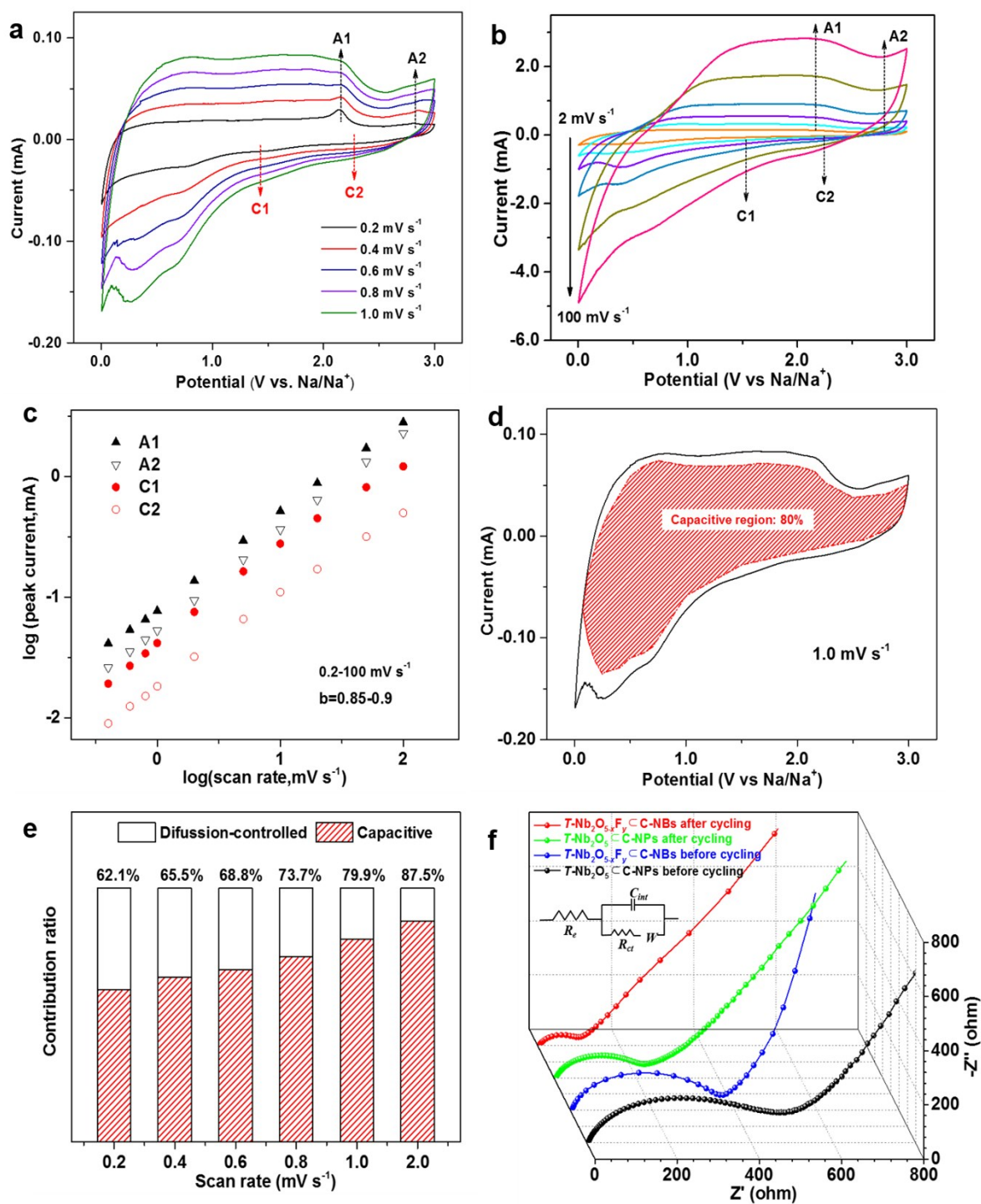


Figure S12. Kinetic analysis of the electrochemical behaviour of $T\text{-Nb}_2\text{O}_{5-x}\text{F}_y/\text{C-NBs}$. **(a, b)** CV profiles at various scan rates from 0.2 to 100 mV s^{-1} . **(c)** b -value determination of the anodic and cathodic peak currents shows the pseudocapacitive charge storage behaviour. **(d)** Capacitive contribution (red shaded area) to the total charge storage at a scan rate of 1.0 mV s^{-1} . **(e)** Contribution ratios of diffusion-controlled and capacitive process at varying scan rates from 0.2 to 2.0 mV s^{-1} . **(f)** Nyquist representation of impedance spectra before and after cycling.

Figures S12a and **S12b** show CV profiles of $T\text{-Nb}_2\text{O}_{5-x}\text{F}_y\text{C-NBs}$ at various scan rates from 0.2 to 100 mV s^{-1} . The cathodic peaks located at 2.4 and 1.5 V were attributed to the stepwise intercalation of sodium ions into the $T\text{-Nb}_2\text{O}_{5-x}\text{F}_y\text{C-NBs}$ host, whereas the anodic peaks centered at 2.1 and 2.7 V arose from the gradual sodium extraction. The peak potentials of the redox peaks *A1*, *A2*, *C1* and *C2* did not shift significantly with sweep rates, indicating their fast charge storage kinetics arising from the pseudocapacitive intercalation.⁵⁻⁶ Based on CV measurements, energy storage properties that characterise diffusion-controlled and surface capacitive mechanisms can be distinguished. Equation 4 below provides a basic analysis for indicating the extent of capacitive effect through analysing the relation between the measured current (*i*) and scan rate (*v*). Assuming the current obeys a power-law relationship with the scan rate leads to:

$$i = av^b \quad (4)$$

$$\log(i) = b \cdot \log(v) + \log\left(\frac{i}{v^b}\right) \quad (5)$$

where *a* and *b* are both adjustable parameters. The exponent, *b*, can be obtained from the slope by plotting $\log(i)$ against $\log(v)$ (Equation 5). A *b*-value of 0.5 would represent a faradaic reaction controlled by semi-infinite linear diffusion, whereas a value of 1 indicates a surface-controlled process.⁷ Note that due to the occurring conversion reaction at the low potentials, the power law is not feasible to evaluate the relationship between the current and the sweep rate at potentials where decomposition happens. Therefore, only the *b*-values of the two pairs of anodic and cathodic peaks *A1*, *A2*, *C1* and *C2* were used to study the kinetics, corresponding to the pseudocapacitive behaviour. **Figure S12c** represents the linear lines of $\log(i)$ versus $\log(v)$ from 0.2 to 100 mV s^{-1} for the two pairs of anodic and cathodic peaks of $T\text{-Nb}_2\text{O}_{5-x}\text{F}_y\text{C-NBs}$. For scan rates ranging from 0.2 to 10 mV s^{-1} , the *b*-values for all of the cathodic and anodic peak currents were quantified to be about 0.9, suggesting that the current response is predominantly surface-controlled. As the sweep rates increased to 20-100 mV s^{-1} , the *b*-value slight decreased from 0.9 to 0.85 for the peaks *A1*, *A2*, *C1* and *C2*. This change in *b*-value is attributed to the increasing effect on rate capability limitation coming from ohmic contribution and/or diffusion constraints.^{5,8} The peak current scales linearly with sweep rate over a broad range of sweep rates, manifesting the pseudocapacitive feature in $T\text{-Nb}_2\text{O}_{5-x}\text{F}_y$.⁹

Moreover, capacitive contribution to the current response was qualitatively measured by separating the current response (*i*) at a fixed potential (*V*) into the capacitive-like (k_1v) and diffusion-controlled processes ($k_2v^{1/2}$) according to

$$i(V) = k_1v + k_2v^{1/2} \quad (6)$$

where k_1 and k_2 are constants at a particular sweep rate. The analysis of $T\text{-Nb}_2\text{O}_{5-x}\text{F}_y\text{-C-NBs}$ indicates that around 80 % of the total current is capacitive-like at a sweep rate of 1.0 mV s^{-1} , which is highlighted in the red area (**Figure S12d**). The result shows that at low potentials, the current response displays a diffusion-dominated behaviour, which is correlated to the conversion reaction of $T\text{-Nb}_2\text{O}_{5-x}\text{F}_y$. Whereas at higher potentials, pseudocapacitance is predominantly contributing to the rapid charge storage. The contribution ratios between the two separate mechanisms at various scan rates are determined in **Figure S12e**. As one increases the rate, the amount of diffusion always decreases because the amount of time is less. The capacitive contribution thus shows a gradually rising trend with an increasing sweep rate and reaches a percentage of 87.5% at 2.0 mV s^{-1} .

Figure S12f shows the Nyquist plots of the $T\text{-Nb}_2\text{O}_{5-x}\text{F}_y\text{-C-NBs}$ before and after 10 cycles over a frequency range from 0.01 Hz to 1 MHz. The circuit model used for fitting is shown in the inset of **Figure S12f**, where R_e is the electrolyte resistance, C_{int} is the interphase capacitance, R_{ct} is the charge transfer resistance at the electrode/electrolyte interface, and W is associated with the ion diffusive Warburg impedance. Simulations indicate that R_{ct} of $T\text{-Nb}_2\text{O}_{5-x}\text{F}_y\text{-C-NBs}$ decreased from 323.5 to 103.6 ohms after cycling. The considerable decrease of charge transfer resistance after sodiation may due to the inserted sodium ions in the lattice, which could increase the electronic conductivity.¹⁰⁻¹¹

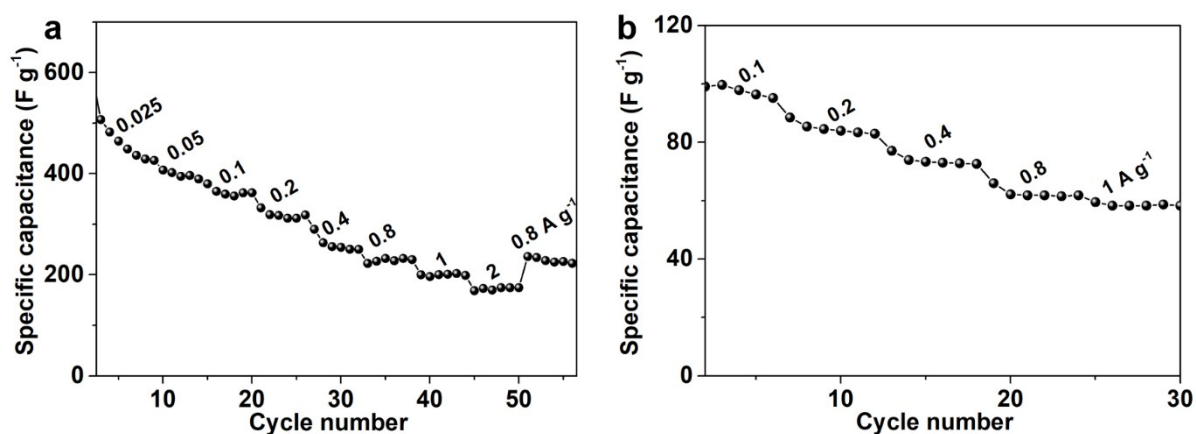


Figure S13. Galvanostatic charge-discharge capacitance of (a) $T\text{-Nb}_2\text{O}_{5-x}\text{F}_y\text{-C-NBs}$ electrode and (b) AC electrode at varying applied current densities.

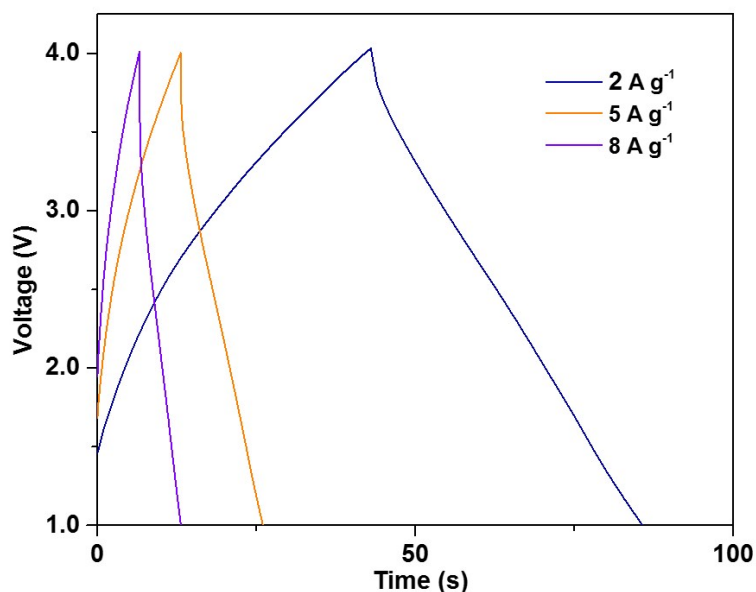


Figure S14. Galvanostatic charge/discharge profiles with triangular shape at high current densities (2, 5 and 8 A g⁻¹) of $T\text{-Nb}_2\text{O}_{5-x}\text{F}_y\text{-C-NBs//AC}$ NIC cell.

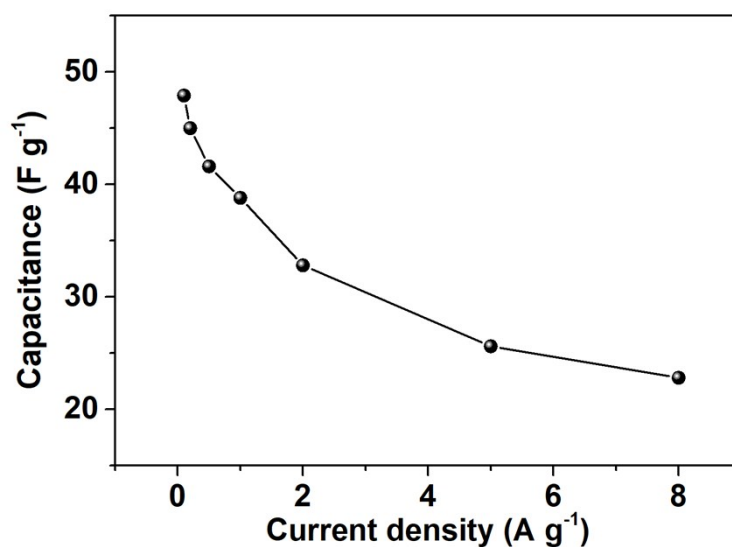


Figure S15. Specific capacitance of the $T\text{-Nb}_2\text{O}_{5-x}\text{F}_y\text{-C-NBs//AC}$ NIC cell at various current densities.

References

1. J. P. Perdew, K. Burke and M. Ernzerhof, *Phys Rev Lett*, 1996, **77**, 3865-3868.
2. B. Delley, *The Journal of Chemical Physics*, 1990, **92**, 508-517.
3. J. P. Perdew, A. Ruzsinszky, G. I. Csonka, O. A. Vydrov, G. E. Scuseria, L. A. Constantin, X. Zhou and K. Burke, *Physical Review Letters*, 2008, **100**, 136406.
4. D. Chen, J.-H. Wang, T.-F. Chou, B. Zhao, M. A. El-Sayed and M. Liu, *Journal of the American Chemical Society*, 2017, **139**, 7071-7081.
5. V. Augustyn, J. Come, M. A. Lowe, J. W. Kim, P.-L. Taberna, S. H. Tolbert, H. D. Abruña, P. Simon and B. Dunn, *Nature Materials*, 2013, **12**, 518.

6. Q. Wei, Y. Jiang, X. Qian, L. Zhang, Q. Li, S. Tan, K. Zhao, W. Yang, Q. An, J. Guo and L. Mai, *iScience*, 2018, **6**, 212-221.
7. J. Wang, J. Polleux, J. Lim and B. Dunn, *The Journal of Physical Chemistry C*, 2007, **111**, 14925-14931.
8. C. Chen, Y. Wen, X. Hu, X. Ji, M. Yan, L. Mai, P. Hu, B. Shan and Y. Huang, *Nature Communications*, 2015, **6**, 6929.
9. V. Augustyn, P. Simon and B. Dunn, *Energy & Environmental Science*, 2014, **7**, 1597-1614.
10. B. Orel, M. Maček, J. Grdadolnik and A. Meden, *Journal of Solid State Electrochemistry*, 1998, **2**, 221-236.
11. M. Maček, B. Orel and U. O. Krašovec, *Journal of The Electrochemical Society*, 1997, **144**, 3002-3010.